

Improving holographic particle characterization by modeling spherical aberration

CAROLINE MARTIN,¹ BRIAN LEAHY,¹ AND VINOTHAN N. MANOHARAN,^{1,2,*}

¹*Harvard John A. Paulson School of Engineering and Applied Sciences, Harvard University, Cambridge MA 02138, USA*

²*Department of Physics, Harvard University, Cambridge MA 02138, USA*

*vnm@seas.harvard.edu

Abstract: Holographic microscopy combined with forward modeling and inference allows colloidal particles to be characterized and tracked in three dimensions with high precision. However, current models ignore the effects of optical aberrations on hologram formation. We investigate the effects of spherical aberration on the structure of single-particle holograms and on the accuracy of particle characterization. We find that in a typical experimental setup, spherical aberration can result in systematic shifts of about 2% in the inferred refractive index and radius. We show that fitting with a model that accounts for spherical aberration decreases this aberration-dependent error by a factor of two or more, even when the level of spherical aberration in the optical train is unknown. With the new generative model, the inferred parameters are consistent across different levels of aberration, making particle characterization more robust.

© 2021 Optical Society of America under the terms of the [OSA Open Access Publishing Agreement](#)

1. Introduction

The combination of digital holographic microscopy, forward modeling, and statistical inference allows colloidal particles to be characterized and tracked with high precision over a large depth of field [1]. In contrast to the traditional method of interpreting holograms by reconstruction [2, 3], where the fields scattered by the object are recovered by physically or numerically shining light through the recorded hologram, in forward-modeling approaches a scattering theory is directly fit to a minimally processed hologram [4, 5]. This approach yields estimates of the particle's three-dimensional position, index of refraction, and size. The forward-modeling approach has the advantage that the position and properties of the object can be inferred directly from the hologram, whereas reconstructions must be further processed to recover this information. When the objects are spheres approximately as large as the wavelength, their reconstructions often do not resemble spheres [6], making it difficult to precisely extract their positions from the reconstruction. Furthermore, the forward-modeling approach yields estimates of the particle's index of refraction, which cannot be directly inferred from a reconstruction. The precision of the quantities inferred from forward-modeling and fitting, combined with the high acquisition speed of the holographic microscope, make the approach useful for many applications, including microrheology [7], visualizing the dynamics of colloidal clusters [8], and studying bacterial swimming [9].

However, the most commonly used forward models ignore optical aberrations, which exist in all imaging systems. Not modeling such aberrations can lead to systematic errors in the inferred parameters. Although many techniques have been demonstrated to correct for the effects of aberrations and artifacts on reconstructions [10–17], there has been little work on accounting for these effects in forward models. Recent models do include the phase effects introduced by an ideal objective lens [1, 18], but they do not include aberrations in either the objective or experimental setup. Moreover, the effects of aberrations on the accuracy of parameters inferred through model-based approaches have not yet been examined.

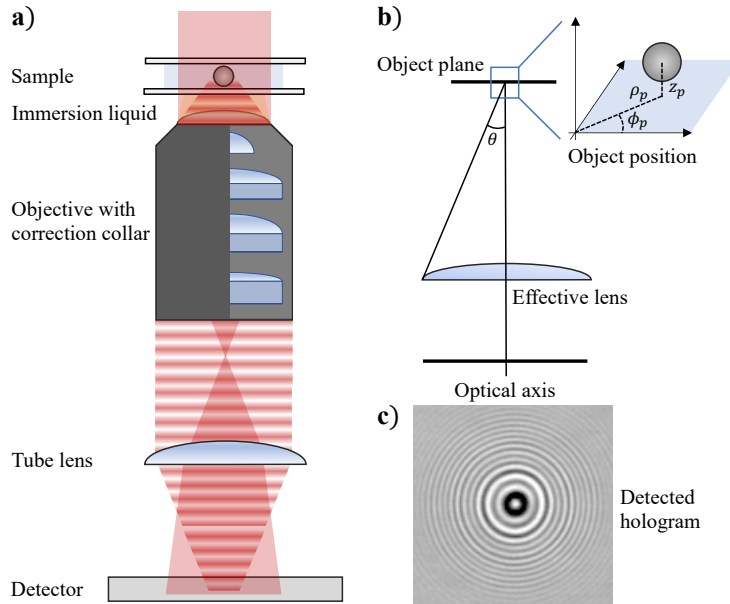


Fig. 1. (a) Diagram of the optical train in a typical in-line digital holographic microscope. Collimated coherent light (red) illuminates a sample chamber consisting of an object in a medium between a glass slide and coverslip. Here, we show an immersion objective with a correction collar. (b) We treat the optical train as a single effective lens pupil with polar angle θ , as defined from the optical axis. The object's position in the object plane is defined by (ρ_p, ϕ_p, z_p) in cylindrical coordinates. (c) A measured hologram from a $1.05\ \mu\text{m}$ polystyrene sphere sitting $7.5\ \mu\text{m}$ above the focal plane, illuminated with $660\ \text{nm}$ light. We record the hologram with a water-immersion lens with a numerical aperture of 1.20 and set the correction collar to minimize aberration.

It is important to understand the effects of aberrations because most microscopy experiments are subject to them. Here, we focus on spherical aberration. Although most high-quality objectives are corrected for spherical aberration near the focus, holographic microscopy is often used to image particles far from the focal plane, where the aberration may be less well corrected. Furthermore, the interface between a liquid sample and a glass coverslip can lead to spherical aberration when the refractive index of the objective immersion fluid is not matched to that of the sample medium [19]. Water-immersion objectives are therefore used to minimize aberrations when aqueous samples are imaged. But even with a water-immersion objective, spherical aberration can be introduced by the coverslip interface. This aberration can be corrected by setting the objective's correction collar, which adjusts the position of a movable central lens group within the objective (Figure 1a), to compensate for the thickness of the coverslip, which is typically $0.10\ \text{mm}$ to $0.20\ \text{mm}$. If the correction collar is set incorrectly, however, spherical aberration is induced. Thus, unless the microscopist carefully measures the thickness of each coverslip—a laborious task when many samples must be imaged—the holograms will likely be subject to spherical aberration. To maximize the precision of tracking and characterization, we must therefore consider the effects of aberrations that can be induced by the experimental setup, as well as those inherent to the objective.

In this article, we experimentally examine the effects of spherical aberration on holograms captured in an in-line holographic microscope and develop a model to describe these aberrations.

We fit this model directly to aberrated holograms and extract information about the particle as well as the aberrations. This method does not require reconstruction or image processing. We find that modeling the effect of aberrations improves agreement between the model predictions and the experimental data, leading to lower residuals between the best-fit holograms and data across levels of induced aberration. We also find that the inferred parameters do not change as the level of aberration in the optical train increases. Modeling the aberrations therefore allows one to more accurately characterize colloidal spheres even if one does not know whether the experimental setup is spherically aberrated, or by how much. The robustness of the fits with this new forward model to aberrations, either induced in or inherent to the optical system, could simplify experiments and reduce systematic errors.

2. Effect of spherical aberration on hologram structure

To explore the effects of typical levels of spherical aberration on hologram structure, we image an immobilized polystyrene microsphere with a reported radius of 1.05 μm (density 1.055 g/mL, index 1.591 at 590 nm, Invitrogen S37500) under varying levels of spherical aberration. To immobilize the microsphere, we fill an inverted sample chamber with a 0.001 % w/v colloidal suspension in a 0.2 mM NaCl aqueous solution. The particles then sediment and stick to the slide, likely because the salt screens any electrostatic repulsion between the sphere and glass. We then reorient the sample chamber. The particles remain immobilized on the top slide, approximately 150 μm above the interface between the bottom slide and immersion lens.

The particles are illuminated with a diode laser (660 nm wavelength, 120 mW power, Opnext HL6545MG) driven at 130 mA (Thorlabs LDC205C). We use a Nikon Eclipse Ti TE2000 microscope with a water-immersion objective and correction collar (Plan Apo VC 60 \times /1.20 WI, Nikon, 300 μm working distance) and a 1024 \times 1024-pixel CMOS monochrome sensor array (PhotonFocus A1024) to capture the hologram. Before analyzing each hologram, we subtract the average of dark-count images taken without illumination and divide the resulting hologram by averaged background images taken with no particles in the field of view. This image processing differs from the double-exposure method of reconstruction-based holography, which removes phase shifts and thus aberrations in the resulting phase-contrast image. We do not attempt to reconstruct the background to obtain a phase map [12]. Instead, our processing method removes stray illumination in the optical train and accounts for non-uniform illumination and artifacts.

We adjust the level of induced spherical aberration by varying the correction collar setting on the objective. The correction collar on our objective corrects for coverslip thicknesses of 0.13 mm to 0.19 mm. Setting the collar to the thickness of the coverslip, measured at 0.17 mm, minimizes spherical aberration; setting it to the furthest available setting, 0.13 mm, maximizes spherical aberration. At the maximally aberrated setting, we expect aberration in the phase from 0.04 mm of glass, which is the difference between the measured and corrected thicknesses. This difference should induce a phase shift $\Delta\phi$ between the paraxial and off-axis rays. For a homogeneous material with refractive index n_2 and thickness h embedded in a medium with refractive index n_1 , $\Delta\phi$ is given by

$$\Delta\phi = hk (n_2 - n_1) \left[2 \frac{n_1}{n_2} \sin^2 \left(\frac{\theta}{2} \right) + 2 (n_2 + n_1) \frac{n_1^2}{n_2^3} \sin^4 \left(\frac{\theta}{2} \right) + \dots \right], \quad (1)$$

where k is the wavenumber and θ is the angle of incidence of the off-axis ray [20]. For a glass layer ($n_2 = 1.515$) with thickness $h = 0.04$ mm surrounded by water ($n_1 = 1.33$), and at the maximum angle of incidence set by the numerical aperture of the lens (NA = 1.2), we calculate a maximum phase shift corresponding to approximately 52 wavelengths. In the above expression, the $\sin^2(\theta/2)$ term corresponds to defocus, which accounts for 35 wavelengths of phase shift, and the $\sin^4(\theta/2)$ term corresponds to the primary spherical aberration, which accounts for

the remaining 17 wavelengths. The higher order terms correspond to higher order spherical aberration. To minimize the aberration induced by the coverslip, we correctly set the correction collar to the precisely measured thickness of the coverslip (0.17 mm). In this case, we expect any remaining aberration to be intrinsic to the optical system, rather than induced by the experimental setup. We note that because high-numerical-aperture objectives are designed to image objects in the focal plane, they may not be well corrected for aberrations far from the focus.

To examine how increasing the aberration affects the hologram structure, we record “stacks” of holograms of the immobilized sphere by sweeping the focus through the particle at three different correction-collar settings. We then examine the x - z cross-sections of these hologram stacks, where each section shows the intensity of the hologram through the central fringe (Figure 2). The particle height determines the spacing of the fringes in the resulting hologram, with the fringe spacing increasing with increasing distance from the focal plane. The x - z cross-sections therefore have a cone-like structure, with a bright center above the focus and a dark center below. With no spherical aberration, we expect a single focal point at which the center of the hologram transitions from bright to dark, which we observe in the cross-section at 0.17 mm correction.

As we change the correction collar setting, the increase in aberration introduces several noticeable changes in the recorded hologram structure. First, oscillations between bright and dark points appear along the central axis (orange arrows in Figure 2), and the number of oscillations increases as we increase the aberration. Second, we observe an overlap of fringes near the focus. Instead of converging at the focal plane, the bottom cone structure converges at a point above the focal plane with increasing aberration, resulting in distortions due to the overlap of the fringes of the top and bottom cone near the focal plane (green arrows in Figure 2). Finally, the position of the focal plane shifts as the aberration increases, as highlighted in Figure 2 by the increasing distance of the focal planes from the blue dotted line.

These changes in structure are the result of the angle-dependent phase shift due to increasing spherical aberration. Spherical aberration changes the phase of the off-axis rays. The interference between these peripheral rays and the paraxial rays produces the bright and dark points that we see in the data; the up-down asymmetry is characteristic of spherical aberration [21]. The overlap of fringes as the cone structures do not come to a single point is also indicative of spherical aberration, as there is no longer a single well-defined focal plane in the presence of these aberrations. Finally, the observed defocus effect is also characteristic of aberration induced by index mismatch, as described above.

3. Modeling the effect of spherical aberration

These results show that spherical aberration caused by small offsets in the correction collar can induce significant changes in the recorded holograms across a wide depth of field. To infer accurate particle parameters under typical levels of spherical aberration, we need a forward model that accounts for these effects.

To model the effects of aberration on a recorded hologram, we build upon the treatment for modeling an unaberrated lens from Leahy, Alexander, and coworkers [18]. In an unaberrated system, all rays emitted from a point source on the focal plane come to a focus at a single point on the detector. By Fermat’s principle, these rays traverse the same optical path length through the imaging system. In an aberrated system, the rays do not come to a focus at a single point, and therefore the phase of each ray differs. These phase aberrations can be quantified by the deviation Φ of each ray’s phase from its ideal value, as measured on the lens pupil. In the presence of general aberrations, Φ depends both on the position on the lens pupil and on the source’s in-plane position [21]. For spherical aberration, however, Φ is a function of the polar angle θ only, defined in Figure 1b. For incident light polarized along the x -direction \hat{x} of the detector plane, propagating the fields through the optical train yields the incident (\mathbf{E}_{in}) and scattered fields

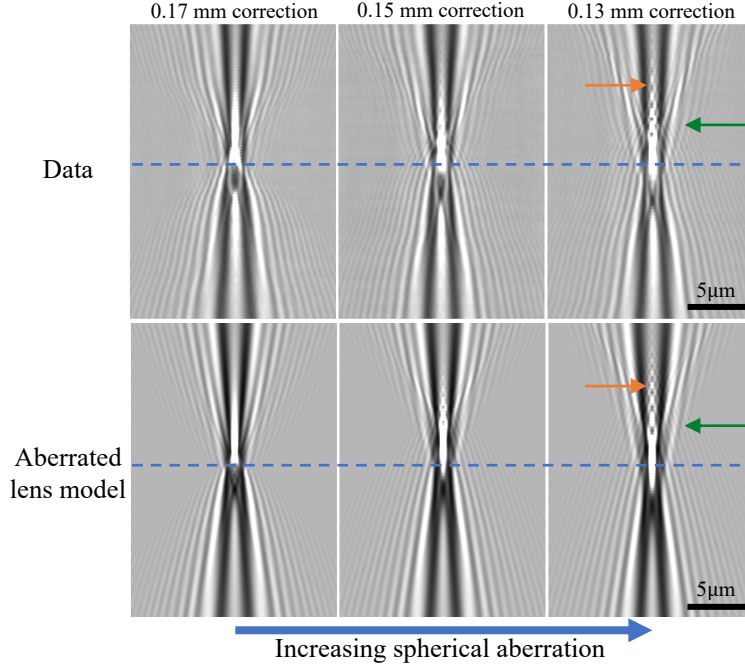


Fig. 2. x - z cross-sections of stacks of holograms of an immobilized $1.05\ \mu\text{m}$ -radius polystyrene microsphere, taken from $15\ \mu\text{m}$ below to $15\ \mu\text{m}$ above the focus in $0.25\ \mu\text{m}$ intervals at three correction collar settings. Adjusting the correction collar induces spherical aberration, which results in on-axis oscillations in brightness (orange arrow), overlapping fringes close to the focal plane (green arrow), and defocus. The blue line marks the focal plane of the least aberrated system; all stacks are taken with the lens in the same physical position. The top row of cross-sections shows experimental data. The bottom row shows calculations from a model that includes spherical aberration. By changing a_0 in the aberration series (primarily fourth order in the phase deviation), we are able to produce cross-sections that capture the distortions in the experimentally observed holograms.

(\mathbf{E}_{sc}) on the detector:

$$\mathbf{E}_{\text{in}} \propto -E_0 e^{i\Phi(0)} \hat{\mathbf{x}} \quad (2)$$

$$\mathbf{E}_{\text{sc}}(\rho_p, \varphi_p, z_p) \propto \frac{E_0}{2} \left\{ \left[\mathcal{I}_0(k\rho_p, kz_p) + \mathcal{I}_2(k\rho_p, kz_p) \cos(2\varphi_p) \right] \hat{\mathbf{x}} + \mathcal{I}_2(k\rho_p, kz_p) \sin(2\varphi_p) \hat{\mathbf{y}} \right\}, \quad (3)$$

where (ρ_p, φ_p, z_p) is the position of the particle in cylindrical coordinates, as shown in Figure 1b, and $\hat{\mathbf{y}}$ is the unit vector along the y direction. We have omitted phase and amplitude factors common to both the incident and scattered fields. In the presence of aberrations, the integrals \mathcal{I}_0 and \mathcal{I}_2 are defined as

$$\mathcal{I}_0(u, v) = \int_0^\beta [S_\perp(\theta) + S_\parallel(\theta)] J_0(u \sin \theta) e^{iv(1-\cos \theta)} e^{i\Phi(\theta)} \sqrt{\cos \theta} \sin \theta \, d\theta \quad (4)$$

$$\mathcal{I}_2(u, v) = \int_0^\beta [S_\perp(\theta) - S_\parallel(\theta)] J_2(u \sin \theta) e^{iv(1-\cos \theta)} e^{i\Phi(\theta)} \sqrt{\cos \theta} \sin \theta \, d\theta, \quad (5)$$

where J_n is the Bessel function of the first kind of order n , S_\perp and S_\parallel are the components of the far-field scattering matrix given by Mie theory, and β is the acceptance angle of the lens.

In the unaberrated-lens model [18], Φ is constant and \bar{I}_0 and \bar{I}_2 are changed only by a phase factor $e^{i\Phi}$ imparted by the lens. In the presence of spherical aberrations, Φ is a general function of θ^2 , and therefore Φ is generally Taylor-expanded as an even polynomial in θ . The constant term in this polynomial corresponds to piston, which is irrelevant for in-line holographic microscopy because it affects the incident and scattered fields identically and therefore does not alter their interference. The quadratic term corresponds to defocus, which is degenerate with z_p . Thus, we represent $\Phi(\theta)$ as a function $(1 - \cos \theta)^2 [a_0 + a_1 P_1(1 - \cos \theta) + a_2 P_2(1 - \cos \theta)]$, where P_ℓ are Legendre polynomials and the coefficients a_ℓ are parameters that describe the level of aberration. Since $1 - \cos \theta = \theta^2/2 - \theta^4/24 + \dots$, this parameterization excludes piston and defocus aberrations. The coefficients a_0 , a_1 , and a_2 allow us to account for fourth- through eighth-order aberrations in the phase (or third- to seventh-order in the ray displacements). While the coefficient a_0 primarily describes fourth-order spherical aberration, the coefficients a_1 and a_2 describe a mix of fourth-, sixth-, and eighth-order aberrations. We choose to parameterize Φ in terms of Legendre polynomials to make it easier to fit the aberration coefficients to data; a parameterization in terms of ordinary polynomials leads to stronger covariances between the inferred expansion coefficients.

With this model for spherical aberrations, we are able to generate holograms that capture the aberrated structure we observe in the data. We generate x - z cross-sections at evenly spaced intervals as z_p moves through the focal plane (Figure 2, bottom), using parameters based on the manufacturer’s specifications of the microsphere imaged in the top row. When the aberration coefficients are set to zero, we recover the expected unaberrated structure: a double cone that comes to a single focus where the hologram center transitions from bright to dark. When we increase the aberrations by increasing a_0 (corresponding to primarily fourth-order phase aberrations), we reproduce the effects we observe in the aberrated data, including the on-axis oscillations in brightness and the overlapping fringe pattern near the focal plane. Because our parameterization of the aberration function separates defocus from spherical aberrations, we also adjust z_p in the generated holograms to account for the defocus in the data.

The model does not capture all of the structure seen in the cross-sections, particularly in the regions near the focal plane. For example, the model does not accurately reproduce the intensity and structure of the dark region below the focus. These discrepancies suggest the need to model other effects, including perhaps other types of aberrations. Nonetheless, our results show that accounting for spherical aberration captures many of the aberration-dependent distortions in hologram structure that can arise under typical experimental conditions.

4. Effect of spherical aberration on particle characterization

To determine how spherical aberrations affect the accuracy of particle characterization, we fit holograms of a single, immobilized 1.05 μm -radius polystyrene sphere at varying coverslip corrections, recorded from 30 μm above to 30 μm below the focus in 0.25 μm intervals. We fit both the aberrated-lens model described above and the unaberrated-lens model [18] (hereafter called the “lens model”) to the measured holograms to infer the particle radius, refractive index, and position, as well as the objective acceptance angle β and the field rescaling parameter α . For the aberrated-lens model, we also fit three coefficients of the aberration series, a_0 , a_1 , and a_2 (see Appendix A for details on how we choose the order of the series required to describe aberrations in the data). We use a Bayesian framework, as described in Appendix A. To avoid local minima in the posterior probability density, we use a combination of nonlinear least-squares fitting, covariance matrix adaptation evolution strategy, and parallel-tempered affine-invariant Markov-chain Monte Carlo sampling.

We find that the aberrated-lens model produces consistently better fits to the data than the lens model, as measured by the sum of squared residuals χ^2 (Figure 3). When the particle is within 5 μm of the focal plane, fitting becomes inconsistent for both models, and the residuals

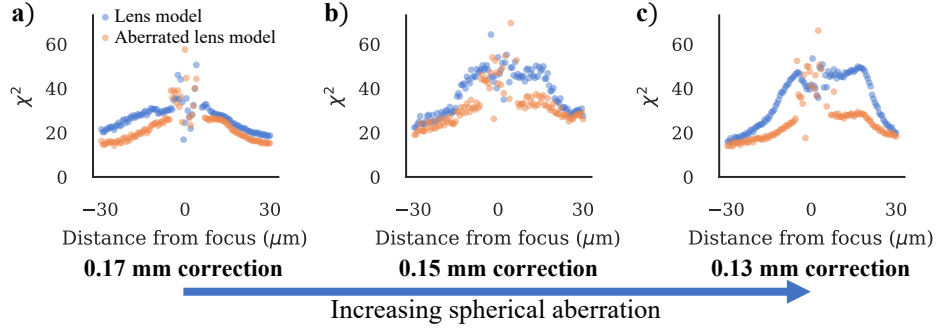


Fig. 3. (a-c) The sum of squared residuals between holograms of an immobilized microsphere and best-fit holograms found with both the lens model and aberrated-lens model as a function of distance from focal plane and level of spherical aberration. While both models produce high residuals near the focal plane, outside this region, the aberrated-lens model produces consistently lower residuals than the lens model does. This improvement in goodness-of-fit occurs across z_p and aberration level, with the largest improvement seen in the most aberrated system.

between the data and best-fit holograms are large. When the particle is $30\ \mu\text{m}$ from the focal plane, both models produce fits with comparable residuals. As the microsphere approaches the focus, however, the residuals found by the lens model increase significantly. Furthermore, the lens model fits the data increasingly poorly as the aberration increases. By contrast, the residuals found by fitting the aberrated-lens model do not increase as sharply with decreasing distance between the microsphere and focal plane and do not change as much with the level of aberration. The aberrated-lens model also produces consistently lower residuals than the lens model, with the largest improvement in goodness-of-fit observed for the most aberrated system. When the particle is farther than $5\ \mu\text{m}$ from the focal plane, we find that modeling the effect of aberrations produces more consistent residuals and improves goodness-of-fit at all aberration levels.

Ignoring the effects of spherical aberration in the model results not only in higher residuals but also in systematic shifts in the inferred particle refractive index and radius with the aberration level. When the particle is more than $5\ \mu\text{m}$ from the focal plane, the inferred values for both the refractive index and radius differ consistently between the most aberrated ($0.13\ \text{mm}$ collar setting) and least aberrated ($0.17\ \text{mm}$) systems, even when the particle is at the same z_p (Figure 4, top). We quantify this parameter shift by determining the absolute difference between the inferred parameters for each z_p more than $5\ \mu\text{m}$ from the focal plane, then averaging across particle position to find the mean absolute difference with standard error. The inferred refractive indices differ by 0.030 ± 0.002 , or $(1.8 \pm 0.1)\%$, and the inferred radii differ by $(0.020 \pm 0.002)\ \mu\text{m}$, or $(2.0 \pm 0.2)\%$, when the particle is more than $5\ \mu\text{m}$ from the focal plane. This difference is far larger than the uncertainty in parameters, estimated as the standard error for each best-fit value and shown as error bars in Figure 4.

When we account for aberration in our model, the inferred parameters no longer depend on the level of aberration (Figure 4, bottom). When the sphere is more than $5\ \mu\text{m}$ from the focal plane, the refractive indices inferred using the aberrated-lens model differ by 0.002 ± 0.001 , or $(0.16 \pm 0.03)\%$, between the most and least aberrated systems, an order-of-magnitude improvement over the refractive indices inferred using the lens model. The inferred radii differ by $(0.007 \pm 0.002)\ \mu\text{m}$, or $(0.8 \pm 0.2)\%$, a two-fold improvement.

Furthermore, the refractive index and radius that we infer by fitting the aberrated-lens model are close to the values reported by the manufacturer of the particles, irrespective of the aberration level. When the microsphere is more than $5\ \mu\text{m}$ from the focal plane, we infer a refractive index

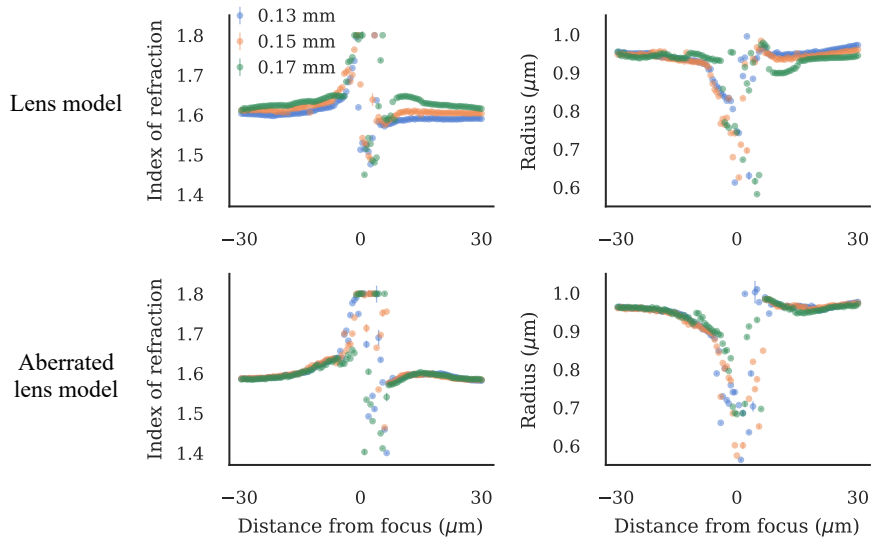


Fig. 4. Refractive index and radius inferred by fitting the lens model and aberrated-lens models to the data, shown as a function of particle distance from the focal plane. Colors indicate the level of spherical aberration, as measured by the correction-collar setting (lowest level of aberration is at 0.17 mm). Both models perform poorly near the focal plane, yielding unphysical and inconsistent values for the refractive index and radius when the particle is closer than about $5\ \mu\text{m}$ to the focus. Outside this region, the refractive index and radius inferred by fitting the lens model depend on the level of aberration in the system. For the aberrated-lens model, this systematic difference disappears, and we obtain consistent results across aberration levels.

of $n = 1.597 \pm 0.014$ and a radius of $r = (0.951 \pm 0.017)\ \mu\text{m}$ for the least aberrated system, and $n = 1.599 \pm 0.015$ and $r = (0.950 \pm 0.027)\ \mu\text{m}$ for the most aberrated system, where the values reported represent the mean and standard deviation of inferred parameters across z_p values. The manufacturer reports the value of the radius as $r = (1.050 \pm 0.026)\ \mu\text{m}$ and the refractive index as $n = 1.591$ at 590 nm; we expect the refractive index of polystyrene to be $n = 1.586$ at 660 nm [22]. We find good agreement between the inferred and expected refractive index irrespective of aberration level in the system. Although there is a difference between the manufacturer's mean value and our inferred value of the radius, the values we infer are consistent across aberration levels. The remaining systematic difference might arise from differences in measurement conditions (dry *versus* aqueous), polydispersity in the particle stock, or additional unmodeled optical effects. Nonetheless, the self-consistency of the parameters and the agreement between the inferred and expected refractive index show that modeling spherical aberration removes one source of systematic error in particle characterization.

These characterization results do not change significantly with z_p when the particle is more than $10\ \mu\text{m}$ from the focus. The variation in the inferred radius, as quantified by the standard deviation across z_p values, is 0.9 %, and that in the inferred refractive index is 0.5 %, as compared to 19.7 % (radius) and 6.0 % (refractive index) when the particle is less than $10\ \mu\text{m}$ from the focus. Neither the lens model nor the aberrated-lens model give consistent or even physically realistic estimates when the particle is within $5\ \mu\text{m}$ of the focus, and in the $5\ \mu\text{m}$ to $10\ \mu\text{m}$ range, the inferred values have a noticeable z_p dependence. For example, as the particle approaches the focus from above, the refractive index is systematically underestimated and the radius is systematically overestimated; the reverse occurs as the particle approaches the focus from below.

Therefore, the forward-modeling approach that we demonstrate should be used with caution when, for example, one must characterize particles that could drift near the focal plane. Future work should focus on modeling other optical effects that are relevant near the focus. We hypothesize that the poor characterization close to the focus arises because there are few fringes and little contrast, limiting the amount of information that could be extracted by fitting. The dependence of the inferred parameters on z_p that we observe might provide some clues about what other effects must be modeled to improve the precision near the focal plane.

There is no additional computational cost to calculating a hologram with the aberrated-lens model compared to the lens model. On a 1.6 GHz Intel Core i5 processor, the aberrated-lens model takes (85 ± 3) ms to generate a 200×200 pixel hologram, while the lens model takes (86 ± 5) ms; these numbers include overhead incurred by the `holopy` package [23]. However, it does take longer to fit the aberrated-lens model to data because it has more parameters than the lens model.

5. Conclusion

Unless carefully corrected, spherical aberration is present in typical holographic microscopes and can significantly affect hologram structure. Spherical aberration can arise in an otherwise corrected system when the correction collar on a water-immersion lens is incorrectly set, or when there are interfaces between media of different refractive indices—for example, when an aqueous sample chamber is imaged using an oil-immersion or air-immersion objective. We have shown that neglecting to account for this aberration leads to inconsistent particle characterization when fitting a forward model to the data.

Adding the effects of spherical aberration to a forward model of hologram formation improves the fit of the model to the data and removes aberration-dependent shifts in the recovered parameters. Fitting with this aberrated-lens model makes particle characterization with holography robust to aberration for both isolated spheres or well-separated collections of spheres [24]. With greater computational resources, it could be expanded to the characterization of other particles, such as clusters and spheroids [1, 25]. The robustness to level of aberration is a useful feature for experiments, because it means that no prior knowledge or characterization of the aberrations is needed. Instead, the aberration coefficients can be fit at the same time as other parameters such as the refractive index and radius. Thus, our method can correct not only the known aberrations in the microscope, such as those induced by the coverslip, but also aberrations that are unknown to the experimentalist because they are intrinsic to the instrument or objective.

An interesting direction for future work is to determine whether modeling the effects of aberration enables reliable particle characterization even with a highly aberrated lens. For example, low-cost holography with a ball lens may be possible. For highly aberrated systems, our methodology could be extended to other types of aberration, including curvature of field or coma.

Appendix A Numerical methods

We evaluate Eqs. 4–5 using the same methods described by Leahy, Alexander, and coworkers [18] for an unaberrated lens. Because spherical aberrations preserve the azimuthal symmetry in Eqs. 4–5, their numerical evaluation carries no additional computational complexity relative to the unaberrated case and retains a computational advantage over the lensless model due to additional numerical optimizations in the lens model [18]. We use the Python package `holopy` [23, 26] to calculate holograms using the lens model [18].

To fit these models, we use a multi-step approach designed to avoid local minima. We first use a parallel-tempered, affine-invariant, Markov-chain Monte Carlo ensemble sampler, as implemented by the Python package `emcee` [27]. We choose uniform priors with bounds set by any physical constraints of the experimental system ($x, y > 0, r > 0, n > 0, 0 < \beta < 1.2, \alpha > 0$). We run this parallel-tempering algorithm at 7 temperatures with 50 walkers for 2000 steps each,

which takes approximately 12 h per hologram on one core. We therefore use parallel tempering to fit only every 20th hologram in each stack.

We then fit the remaining intermediate holograms using the maximum *a posteriori* parameters found with parallel tempering as the initial guess. We fit these holograms iteratively with the evolution strategy CMA-ES (covariance matrix adaptation evolution strategy) [28], as implemented by the Python package `cma` [29], and with a Levenberg-Marquardt algorithm for nonlinear least-squares fitting, as implemented by the python package `lmfit` [30]. We find that when we fit with CMA-ES alone, we avoid local minima but often fail to fully converge on the minimum within a reasonable computation time. Conversely, we find that when we use only Levenberg-Marquardt least-squares fitting, we converge to a good fit only with a very good initial guess. Thus, we first explore the posterior landscape with CMA-ES, and then ensure that we converge on the best fit through least-squares minimization of the residuals. The combination of the two algorithms with the initial guess from MCMC produces fits comparable to those we find with parallel-tempering, but with much shorter run times. When we maximize the posterior with CMA-ES, we choose broad Gaussian priors, with means set by the maximum *a posteriori* parameters found by parallel tempering and variances set to physically reasonable values, such as the width of a pixel for the particle's x and y coordinates ($\sigma_{x,y} = 0.176 \mu\text{m}$, $\sigma_z = 4 \mu\text{m}$, $\sigma_n = 0.2$, $\sigma_r = 0.1 \mu\text{m}$, $\sigma_\alpha = 0.5$, $\sigma_\beta = 0.4$, $\sigma_{a_\ell} = 300$). The widest priors are chosen for a_0 , a_1 , and a_2 , which have widths of the same order as the typical values we infer for the coefficients. We choose these wide priors because in typical experiments the microscope user has little *a priori* knowledge of the aberration. For other parameters, we place bounds on the Gaussian priors if there are any physical constraints ($x, y > 0$, $r > 0$, $n > 0$, $0 < \beta < 1.2$, $\alpha > 0$). We then use least-squares fitting to minimize the residuals between the data and the best-fit holograms found by CMA-ES. The error bars shown in Figure 4 are calculated by `lmfit` from the estimated covariance matrix. Because the holograms are analyzed individually, the uncertainties are independent. They do not account for systematic errors. We find that when the holograms are closely spaced in z_p , the parameters change slowly enough that we avoid local minima in fitting the holograms between the select parallel-tempered frames.

To determine the order of the expansion of the aberration function necessary to describe the data, we calculate the sum of squared residuals χ^2 and the maximum *a posteriori* parameters for increasing aberration order using the parallel-tempered sampler described above. We select holograms taken at $z_p = 7.5 \mu\text{m}$ above the focal plane, for 0.13 mm to 0.17 mm correction. Holograms at this position are well within the distance from the focus where fitting returns reasonable residuals for all models, but they also show a large change in structure as we change the level of aberrations, indicating a strong dependence on the aberration function. We find that the χ^2 value decays with increasing aberration expansion order, with χ^2 at a maximum with zeroth-order aberration (lens model) and decreasing with each additional aberration order included before plateauing. We observe this decay in χ^2 for all levels of aberration, with the sharpest decay occurring in the most aberrated system. For our data, the χ^2 values plateau when we expand up to the eighth-order phase polynomial, which includes aberration coefficients a_0 , a_1 , and a_2 . We find very small differences between the eighth-order and tenth-order expansion, with an average decrease in χ^2 of 0.6% across levels of aberration. This improvement in goodness-of-fit is much smaller than the 43% mean decrease in χ^2 found between the zeroth- and eighth-order expansion.

We see additional evidence favoring the eighth-order expansion in the comparison of the inferred maximum *a posteriori* parameters to the manufacturer's specifications for the particles. We find that when we include only a_0 in the expansion, the χ^2 value decreases greatly compared to the lens-model, but the maximum *a posteriori* parameters become unphysical, with the maximum *a posteriori* refractive index jumping to nearly 1.68, much larger than the anticipated value of 1.59. As we increase the number of aberration coefficients, the maximum *a posteriori* values of

the parameters plateau to physical values with the eighth-order expansion with coefficients a_0 , a_1 , and a_2 . We find small differences between characterization with the eighth- and tenth-order expansion, with average differences of 0.5 % in refractive index and 0.6 % in radius. To avoid unnecessary complexity in the model, we choose to expand the aberration function to the eighth-order phase polynomial and include three aberration parameters in the model.

Although we find that truncating the aberration series at the eighth-order phase polynomial is appropriate for the aberration level in our experimental system, other experimental systems may require higher-order expansions to fully capture the aberration function.

Funding

This work is partially supported by the National Science Foundation through the Harvard University Materials Research Science and Engineering Center under grant numbers DMR-1420570 and DMR-2011754. Additional support was provided by the Department of Defense through the National Defense Science and Engineering Graduate Fellowship (NDSEG).

Acknowledgments

We thank R. Alexander and S. Barkley for useful discussions on fitting methods.

Disclosures

The authors declare no conflicts of interest.

Data availability

Data from the experiments shown in this paper are available in Ref. 31. Source code for the forward model and inference calculations is available in Ref. 26.

References

1. R. Alexander, B. Leahy, and V. N. Manoharan, "Precise measurements in digital holographic microscopy by modeling the optical train," *Journal of Applied Physics* **128**, 060902 (2020).
2. D. Gabor, "A New Microscopic Principle," *Nature* **161**, 777–778 (1948).
3. U. Schnars and W. P. O. Jüptner, "Digital recording and numerical reconstruction of holograms," *Measurement Science and Technology* **13**, R85–R101 (2002).
4. B. Ovrn and S. H. Izen, "Imaging of transparent spheres through a planar interface using a high-numerical-aperture optical microscope," *JOSA A* **17**, 1202–1213 (2000).
5. S.-H. Lee, Y. Roichman, G.-R. Yi, S.-H. Kim, S.-M. Yang, A. van Blaaderen, P. van Oostrum, and D. G. Grier, "Characterizing and tracking single colloidal particles with video holographic microscopy," *Optics Express* **15**, 18275–18282 (2007).
6. Y. Pu and H. Meng, "Intrinsic aberrations due to Mie scattering in particle holography," *J. Opt. Soc. Am. A* **20**, 1920–1932 (2003).
7. F. C. Cheong, S. Duarte, S.-H. Lee, and D. G. Grier, "Holographic microrheology of polysaccharides from *Streptococcus mutans* biofilms," *Rheologica Acta* **48**, 109–115 (2009).
8. J. Fung and V. N. Manoharan, "Holographic measurements of anisotropic three-dimensional diffusion of colloidal clusters," *Physical Review E* **88**, 020302 (2013).
9. A. Wang, R. F. Garmann, and V. N. Manoharan, "Tracking *E. coli* runs and tumbles with scattering solutions and digital holographic microscopy," *Optics Express* **24**, 23719–23725 (2016).
10. A. Stadelmaier and J. H. Massig, "Compensation of lens aberrations in digital holography," *Optics Letters* **25**, 1630–1632 (2000).
11. S. Grilli, P. Ferraro, S. D. Nicola, A. Finizio, G. Pierattini, and R. Meucci, "Whole optical wavefields reconstruction by Digital Holography," *Optics Express* **9**, 294–302 (2001).
12. P. Ferraro, S. D. Nicola, A. Finizio, G. Coppola, S. Grilli, C. Magro, and G. Pierattini, "Compensation of the inherent wave front curvature in digital holographic coherent microscopy for quantitative phase-contrast imaging," *Applied Optics* **42**, 1938–1946 (2003).
13. T. Colomb, E. Cuche, F. Charrière, J. Kühn, N. Aspert, F. Montfort, P. Marquet, and C. Depeursinge, "Automatic procedure for aberration compensation in digital holographic microscopy and applications to specimen shape compensation," *Applied Optics* **45**, 851–863 (2006).

14. S. D. Nicola, A. Finizio, G. Pierattini, D. Alfieri, S. Grilli, L. Sansone, and P. Ferraro, "Recovering correct phase information in multiwavelength digital holographic microscopy by compensation for chromatic aberrations," *Optics Letters* **30**, 2706–2708 (2005).
15. T. Nguyen, V. Bui, V. Lam, C. B. Raub, L.-C. Chang, and G. Nehmetallah, "Automatic phase aberration compensation for digital holographic microscopy based on deep learning background detection," *Optics Express* **25**, 15043–15057 (2017).
16. N. Verrier, C. Fournier, L. Méès, and T. Fournel, "In-line particle holography with an astigmatic beam: setup self-calibration using an inverse problems approach," *Appl. Opt.* **53**, G147–G156 (2014).
17. L. Denis, C. Fournier, T. Fournel, and C. Ducottet, "Twin-image noise reduction by phase retrieval in in-line digital holography," in "Wavelets XI," , vol. 5914, M. Papadakis, A. F. Laine, and M. A. Unser, eds., International Society for Optics and Photonics (SPIE, 2005), vol. 5914, pp. 148 – 161.
18. B. Leahy, R. Alexander, C. Martin, S. Barkley, and V. N. Manoharan, "Large depth-of-field tracking of colloidal spheres in holographic microscopy by modeling the objective lens," *Optics Express* **28**, 1061–1075 (2020).
19. S. Hell, G. Reiner, C. Cremer, and E. H. K. Stelzer, "Aberrations in confocal fluorescence microscopy induced by mismatches in refractive index," *Journal of Microscopy* **169**, 391–405 (1993).
20. C. J. R. Sheppard and C. J. Cogswell, "Effects of aberrating layers and tube length on confocal imaging properties," *Optik* **87**, 34–38 (1991).
21. M. Born and E. Wolf, *Principles of Optics* (Cambridge University, 1983), 3rd ed.
22. X. Ma, J. Q. Lu, R. S. Brock, K. M. Jacobs, P. Yang, and X.-H. Hu, "Determination of complex refractive index of polystyrene microspheres from 370 to 1610 nm," *Physics in Medicine and Biology* **48**, 4165–4172 (2003).
23. S. Barkley, T. G. Dimiduk, J. Fung, D. M. Kaz, V. N. Manoharan, R. McGorty, R. W. Perry, and A. Wang, "Holographic Microscopy With Python and HoloPy," *Computing in Science Engineering* **22**, 72–82 (2020).
24. J. Fung, R. W. Perry, T. G. Dimiduk, and V. N. Manoharan, "Imaging multiple colloidal particles by fitting electromagnetic scattering solutions to digital holograms," *J. Quant. Spectrosc. Radiat. Transfer* **113**, 2482–2489 (2012).
25. D. W. Mackowski and M. I. Mishchenko, "Calculation of the T matrix and the scattering matrix for ensembles of spheres," *J. Opt. Soc. Am. A* **13**, 2266–2278 (1996).
26. R. Alexander, S. Barkley, T. G. Dimiduk, J. Fung, A. M. Goldfain, D. M. Kaz, B. Leahy, V. N. Manoharan, R. McGorty, R. W. Perry, and A. Wang, "HoloPy: Holography and light scattering in Python," (2021). Source code available at <http://github.com/manoharan-lab/holopy>.
27. D. Foreman-Mackey, D. W. Hogg, D. Lang, and J. Goodman, "emcee: The MCMC Hammer," *Publications of the Astronomical Society of the Pacific* **125**, 306 (2013).
28. N. Hansen and A. Ostermeier, "Adapting arbitrary normal mutation distributions in evolution strategies: The covariance matrix adaptation," in "Proceedings of IEEE international conference on evolutionary computation," (IEEE, 1996), pp. 312–317.
29. N. Hansen, Y. Akimoto, and P. Baudis, "CMA-ES/pycma: r3.0.3," Zenodo (2020). <https://dx.doi.org/10.5281/zenodo.3764210>.
30. M. Newville, T. Stensitzki, D. B. Allen, and A. Ingargiola, "LMFIT: Non-Linear Least-Square Minimization and Curve-Fitting for Python," Zenodo (2014). <https://doi.org/10.5281/zenodo.11813>.
31. C. Martin, B. Leahy, and V. N. Manoharan, "Data for 'Improving holographic particle characterization by modeling spherical aberration'," <https://doi.org/10.7910/DVN/K2A0WW>, Harvard Dataverse, V1 (2021).